Response to reviewer (comment-to-author)

We thank the reviewer for taking the time to provide us with helpful comments that we believe have substantially improved our paper. We address each concern of the reviewer on a point-by-point basis as follows:

1) Eqs. (3): the right hand side does not include "j" which appears in the left hand side. Maybe "ri" means "rij". Please improved the expression.

Reply: The expression was corrected (Page 4 Line 11)

2) Eqs. (4)-(6): The equations are hypothetical and the physical meanings are not well described. For example, what is the basis of assumption of "d1" can be defined by three times larger than the grid size "l", even when there is no specification of the value of "l" in the manuscript. This editor feels such hypothetical relations can be introduced in a paper in the situation of no past similar studies are there, but at least the authors should put more explanation, especially for physical meanings of the assumption.

Reply: Some sentences were added for the background and explanation regarding physical meaning of our approach (Page 4 Line 1-4) and some sentences were modified (Page 4 Line 8-9, 24-26).

3) page 8, line 10 (30?): It will be useful for reader to see the value of the complex refractive index at 532nm with those values at other two wavelengths, because the results are sometimes given for 532nm in Figs. 5-9.

Reply: A table for refractive index was added (Table 1).

4) Figs. 6, 8: It will be useful to show at which size the DDA is connected with FDTD to study the consistency of the computed values by the two methods.

Reply: In the numerical environment of our non-parallel computation, light scattering calculations performed using FDTD were faster than those using DDA for AST-B particles (Nos.10–13). The same sentence was added in the text (Page 6 Line 27-28).

5) Also equivalent homogeneously mixed sphere case can be added for how the internal mixture of BC and WS is different from the usual Mie sphere case.

Reply: For comparison, results of MG and CS for lidar ratios were added (Fig. 8-9).

6) page 10: A table to summarize the values of optical cross sections will be useful for readers to see dependences of discussed parameters on the wavelengths.

Reply: Although we tried to make the table, we gave up because it would be a very large table. For example, 10 (bare soot size) x 5 (mixing state) x 3 (wavelength) x 2 (cross sections Cext, Cabs) = 300 data is necessary for the table of type-A particles. For type-B particles, another table of 390 data is needed. We would like to upload the data files as a supplement together with our final manuscript.

Response to reviewer (RC1)

We thank the reviewer for taking the time to provide us with helpful comments that we believe have substantially improved our paper. We address each concern of the reviewer on a point-by-point basis as follows:

1) The descriptions on the iteration procedure for calculating mixed soot particles are difficult to understand. How many iterations are necessary to obtain Wr=20? What is the relationship between relative humidity and Wr? What is the relative humidity in Figs. 7-9?

Reply: To produce $V_r \sim 20$ particles, we started from the state of bare soot ($V_r = 0$) and the result of particle shape was outputted when V_r exceeded 20. As described in Eq. (3), ~2 % of the surface points defined in the grid space are adhered as WS material for one iteration (including two steps). Approximately, 1000 (2000) iterations were applied for making the $V_r \sim 10$ ($V_r \sim 20$) particle. A sentence was added in the text (Page 5 Line 13-14). The relative humidity is a parameter to determine the refractive index of water soluble (WS). We used the results of refractive index at relative humidity 50% for the plots of section 3. For the dataset of light scattering properties, we calculated the optical properties of particles for 4 cases of relative humidity (0%, 50%, 90%, 98%). The values of relative humidity and refractive indices were mentioned in the text (Page 7 Line 8-9) and in the caption of Table 1.

2) Lidar ratio values should be discussed in more details. Lidar ratio values at 355 nm and 532 nm reported in observational studies should be summarized. In my understanding, the observed lidar ratio at 355 nm was smaller than 532 nm in forest fire cases. It looks the wavelength dependence in Fig. 8 is opposite for small Wr. However, it looks good for large Wr, for example, A-7 Wr=20. The depolarization ratios are also close to the observation, in this case. Considering the lidar ratio values, it may be more appropriate to consider large Wr, even if the depolarization ratios are not well reproduced. Lidar ratios calculated with MG and CS should be also presented.

Reply: Results of lidar ratios for MG and CS were added (Fig.8-9). We also

added a short discussion about the results of lidar ratio (Page 8 Line 18-25, Page 9 Line 13-21) including the results of depolarization ratios. As the reviewer pointed out, lidar ratio at 355 nm can be smaller than that at 532 nm depending on the size and mixing condition of the particle.

Response to reviewer (RC2)

We thank the reviewer for taking the time to provide us with helpful comments that we believe have substantially improved our paper. We address each concern of the reviewer on a point-by-point basis as follows:

1) Is Eq. (1) necessary? Remove it, if it is unnecessary.

Reply: The equation was removed from the manuscript.

2) The discussion on the efficiency of computational methods only focuses on the shape aspect. Actually, the refractive index has large impact on the efficiency comparison between FDTD and DDA.

Reply: A sentence was modified and reference Yurkin et al. (2007) was added (Page 6 Line 19-20).

3) It might be better to have a table of the refractive indices at the 10 wavelengths.

Reply: A table for the refractive index was added (Table 1). Because we only showed the plots for the results of 3 wavelengths (wavelengths for lidar measurements) with one relative humidity (50 %) for water soluble, the refractive indices were listed only for the corresponding 3 wavelengths to avoid the reader's confusion.

4) A reference is required for the Maxwell-Garnett mixing rule.

Reply: Reference was added (Page 7 Line 11).

5) The results are presented for single particles. It is unclear to obtain the size averaged results from the simulated results. More discussion is required on the comparison between simulations and observations/measurements.

Reply: In the revised manuscript, we expanded the part of discussion in

section 3 and in summary. We are preparing another paper regarding the retrieval of soot particles from satellite measurements by using size averaged optical properties. We would like to discuss this issue in our future work if we obtain the reviewer's approval.

6) In summary, it might be better to summarize the new knowledge gained from the present modeling study.

Reply: Our new findings about single scattering properties were summarized (Page 13 Line 1-14).

Response to reviewer (SC1)

We thank the reviewer for taking the time to provide us with helpful comments that we believe have substantially improved our paper.

• For larger aggregates with a high amount of coating the calculated depolarisation ratios for both 355 and 532 nm exceed 0.3, which appears to be too high for soot particles. Some of the modelled particles even give depolarisation ratios, which are higher than 0.5, which is higher than what would be expected of any type of atmospheric aerosol.
• When considering aerosol size distributions for remote sensing applications these high values pose the risk of overestimating the depolarisation ratios with your shape model. A similar effect has been reported by Kahnert, 2017.
• A possible explanation was that the coated soot particles were too non-spherical. Your results point into a similar direction, as some of the soot aggregates with Vr=20 have a smaller depolarisation ratios than the same aggregates with Vr=10. In Kanngießer and Kahnert, 2018 we showed that the speed of transition from film coating to spherical growth is a morphological parameter which has a strong impact on the depolarisation ratio. Having a faster transition to spherical growth resulted in more spherical paticles which had a smaller depolarisation ratio.

Reply: Many thanks for very important comments and information. We essentially agree with the reviewer's opinion. In the revised manuscript, sentences of the same meaning and references were added (Page 9 Line 15-21, Page 13 Line 9-14).

Does your model allow for a more spherical shape for coatings of larger aggregates with e.g. Vr=10? The lab experiments conducted by Pei et al., 2018 suggest that with the application of coating material the soot aggregates become compacted before there will be a growth in particle size. Could the different particle types (AST-A and AST-B) represent such compaction?

Reply: In the revised manuscript, results of lidar ratios for Maxwell-Garnett

(MG) spheres and Core-Shell (CS) spheres were included (Figs 8-9). Approximately, lidar ratios for AST-A and -B particles were in between the results of MG and CS. The modeling and light scattering calculations for more compact soot aggregates than Type-B are possible. We think that the results will be similar to those of CS model. However, we did not carry out these calculations because the results of backscattering properties will show the same fluctuating feature as those of CS particles (Fig. 8-9), and because we have to implement many DDA/FDTD calculations to show general tendency.

A shape model of internally mixed soot particles derived from artificial surface tension

Hiroshi Ishimoto[1], Rei Kudo[1], Kouji Adachi[1]

[1]Meteorological Research Institute, Tsukuba, 305-0052, Japan

5 *Correspondence to*: Hiroshi Ishimoto (hiroishi@mri-jma.go.jp)

Abstract.

To retrieve the physical properties of aerosols from multi-channel ground-based/satellite measurements, we developed a shape model of coated soot particles and created a dataset of their optical properties. Bare soot particles were assumed to have an aggregate shape, and two types of aggregates with different size–shape dependences were modeled using a polyhedral Voronoi

10 structure. To simulate the detailed shape properties of mixtures of soot aggregates and adhered water-soluble substances, we propose a simple model of surface tension derived from the artificial surface potential. The light-scattering properties of the modeled particles with different volume fractions of water-soluble material were calculated using the finite-difference time-domain method and discrete-dipole approximation. The results of the single-scattering albedo and asymmetry factors were compared to those of conventional internally mixed spheres (i.e., effective medium spheres based on the Maxwell–Garnett

15 approximation and simple core–shell spheres). In addition, the lidar backscattering properties (i.e., lidar ratios and linear depolarization ratios) of the modeled soot particles were investigated. For internally mixed soot particles, the lidar backscattering properties were sensitive to the shape of the soot particles and the volume mixing ratio of the assumed water-soluble components. However, the average optical properties of biomass smoke, which have been reported from in situ field and laboratory measurements, were difficult to explain based on the individually modeled particle. Nonetheless, our shape

20 model and its calculated optical properties are expected to be useful as an alternative model for biomass smoke particles in advanced remote sensing via multi-channel radiometer and lidar measurements.

1 Introduction

During the atmosphere aging process of emitted combustion products, soot particles tend to become hydrophilic and form mixtures with weakly light-absorbing materials (Mikhailov et al., 2006)(Adachi et al., 2007)(Moteki and Kondo, 2007)

25 (Shiraiwa et al., 2007)(Adachi and Buseck, 2008)(Shiraiwa et al., 2010). Because of significant enhancements in light absorption and scattering, it has been suggested that soot particles in a mixing state are the second-most important contributor to global warming after carbon dioxide (Jacobson, 2001)(Ramanathan et al., 2008). For climate monitoring and numerical prediction via atmospheric data assimilation, precise estimation of the amount of mixed soot particles and the fraction of soot (black carbon) from satellite-/ground-based remote-sensing measurements is important (Kahnert et al., 2013). Thus,

30 understanding the optical properties of internally mixed soot particles is essential to improve the retrieval accuracy of atmospheric soot particles (Hara et al., 2018). The light-scattering properties of internally mixed particles depend strongly on the complex refractive index of each mixing component. Furthermore, the shape of the incorporated soot particles and overall particle shape in the mixing state significantly alter some of the scattering properties. In particular, particle shape is important for the interpretation of lidar backscattering measurements. Many shape models have been proposed for internally mixed soot

35 particles and their light-scattering properties using the discrete-dipole approximation (DDA) and T-Matrix methods (Adachi et al., 2010)(Scarnato et al., 2012)(Cheng et al., 2014)(Dong et al., 2015)(Liu et al., 2016)(Mishchenko et al., 2016) (Moteki, 2016) (Wu et al., 2016)(Wu et al., 2017) (Kahnert, 2017) (Zhang et al., 2017) (Luo et al., 2018). However, the relationship between mixing state/morphology and light-scattering properties is not well defined.

1

As an alternative model for soot particles in a mixing state, we developed a new shape model of internally mixed particles. We assumed that bare soot particles with fractal-like shapes were mixed with water-soluble (WS) components. Moreover, we considered hydrophilic soot particles with high wettability due to atmospheric aging. The shapes of the mixed particles were determined by applying artificial potential calculations of the surface tension of the WS components. The numerical results of the light-scattering properties of the modeled particles at visible and near-infrared wavelengths are discussed.

## 2 Shape model of internally mixed aerosols

2.1 Soot model

Bare soot particles are commonly described as fractal aggregates formed from primary particles (or monomers) with a degree of overlapping and necking between neighboring primary particles (Yon et al., 2015)(Okyay et al., 2016). Primary particles have a diameter of 20–50 nm (Bond and Bergstrom, 2006), and the fractal dimension of the aggregates depends on emissions conditions and atmospheric aging. For example, newly generated soot aggregates often form lace-like structures with relatively small fractal dimensions, whereas aged soot aggregates tend to be compact and to be characterized by large fractal dimensions (Mikhailov et al., 2001)(Mikhailov et al., 2006)(Zhang et al., 2016). In this study, we modeled soot aggregates using spatial Poisson–Voronoi tessellation. The basic methods to make the aggregate model are the same as those of dust particles and ice aggregates described in our previous works (Ishimoto et al., 2010)(Ishimoto et al., 2012a)(Ishimoto et al., 2012b) (Baran et al., 2018). A spatial Poisson–Voronoi tessellation was produced from randomly distributed nucleation points in the numerical field, and polyhedral cells overlapping with the assumed fractal frame were selected from the tessellation (Ishimoto et al., 2012a). We regarded the cells (i.e., Voronoi cells) as the primary soot aggregate particles to mimic overlapping and necking between neighboring primary particles. To ensure that the size of the Voronoi cells was relatively uniform, we applied a Matérn hard-core point field (Ohser and Mücklich, 2000) to the spatial distribution of the nucleation points (Ishimoto et al., 2012b). Aggregate particles of different sizes were produced in the same manner but by changing the relative size of the fractal frame within the same tessellation. Figure 1 shows two sets of aggregate particles (Types A and B) created from fractal frames of different shapes. To calculate the light-scattering properties, Type A aggregates of 10 sizes and Type B aggregates of 13 sizes (where Nos. 1, 2, and 3 were used for both sets) were prepared. The mean radius of the primary particle $a = 20$ nm was used as a typical value (Wu et al., 2015) (Wu et al., 2017)(Mishchenko et al., 2016)(Luo et al., 2018), and the total size of each aggregate was corrected by adjusting the average cell volume of the aggregate as $V_{c,\text{agg}} = 4/3\pi a^3$. Although the aggregates shown in Figure 1 were created using a box-counting approach to maintain a fractal relationship between size and shape, this fractal relationship differed from that of the commonly used fractal dimension D_f used to describe individual soot particles. The fractal dimension D_f is defined from the number of monomers N, fractal prefactor k_0, and gyration radius R_g as follows (Adachi et al., 2007)

$$N = k_0 \left(\frac{R_g}{a}\right)^{D_f}. \qquad (1)$$

For numerical simulation of the light-scattering properties of aged soot particles, various D_f values for a typical prefactor of $k_0 = 1.2$ have been proposed in the literature, such as $D_f = 2.0 - 2.5$ (Nyeki and Colbeck, 1995), $1.9 - 2.6$ (Adachi et al., 2007), 2.5 (He et al., 2015), 2.6 (Mishchenko et al., 2016), and $2.5 - 3.0$ (Zhang et al., 2017). The corresponding D_f values for our modeled soot particles derived from the calculation of R_g are plotted in Figure 2. Applying the fractal prefactor $k_0 = 1.2$ resulted in aggregate particles in the range of $D_f = 1.9 - 2.5$ (Type A) and $2.5 - 3.0$ (Type B) given a normalized gyration radius of $\ln(R_g/a) \leq 3.6$.

2

Type-A   Type-B
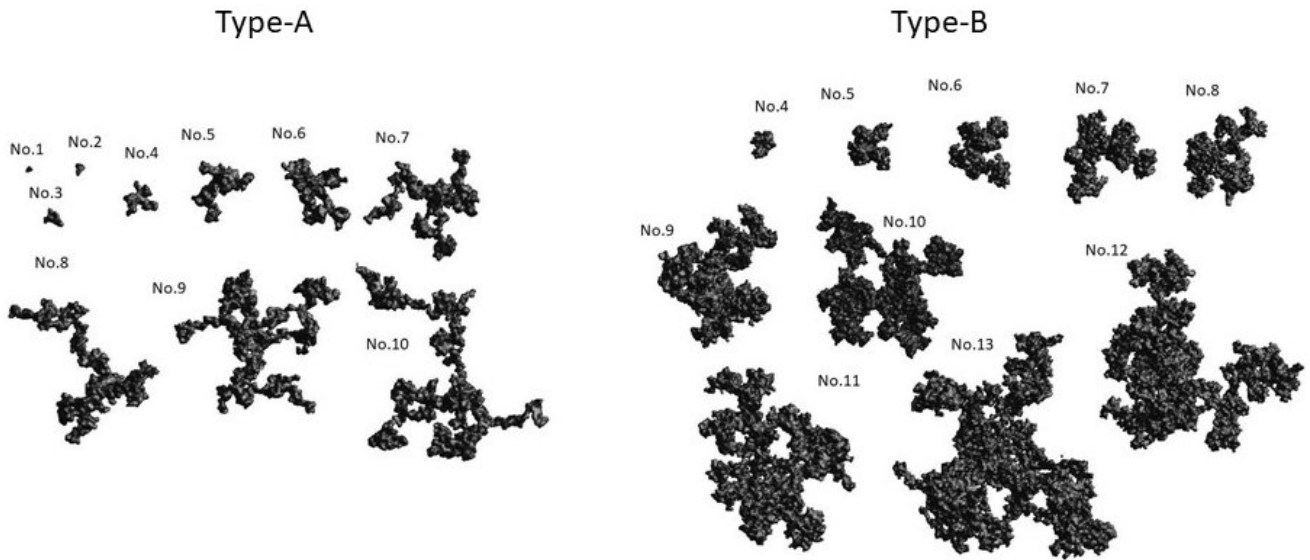
Figure 1. Model of bare soot particles created using three-dimensional Voronoi tessellation (Types A and B).
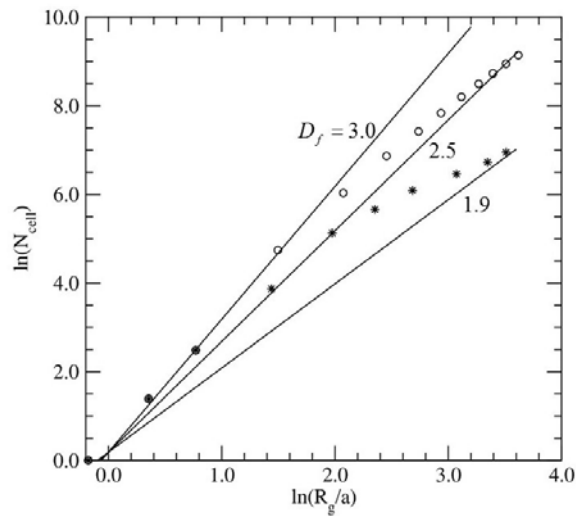
Figure 2. Relationship between the number of cells N_{cell} (assuming $N_{cell} = N$, from Eq. (1) and normalized gyration radius R_g/a for the modeled soot aggregates. Asterisks and open circles correspond to Type A and Type B aggregates, respectively. Solid lines represent the relationship described by Eq. (1) for fractal dimensions of $D_f = 1.9, 2.5, 3.0$ when $k_0 = 1.2$.

2.2 Artificial surface tension of mixed soot and water-soluble components

According to microscopic images of internally mixed soot particles, soot particles are often entirely encapsulated in a spherical shell and completely covered by WS components (Reid and Hobbs, 1998)(Reid et al., 2005a). Thus, WS components behave like a liquid on the particle surface, and the surface tension of WS components is important to describing the overall shapes of

mixed particles. <mark>Surface tension is the result of inter-molecular forces at the microscopic scale, described as the Lennard–Jones potential (Becker et al., 2014). Although some approaches to simulate surface tension in a discrete particle system, such as smoothed particle hydrodynamics (SPH), have been proposed (Tartakovsky and Meakin, 2005) (Leinonen and von Lerber, 2018), a general approach to reproduce the variety of fluid effects has not yet been developed (Akinci et al., 2013).</mark> In this study, we examined a virtual and simple potential field on the surface of the modeled particle to simulate the morphological effects of surface tension. We assumed that the dynamic behavior of liquid could be simulated by the movement of liquid elements from locations of high potential to locations of low potential. From a simple molecular-scale explanation of surface tension, the potential at a surface point becomes smaller as the number of surrounding molecules increases. <mark>The modeled particles were projected in a three-dimensional Cartesian grid space to define surface points for the potential calculations.</mark> The artificial surface potential was defined as an analog of the microscopic surface potential.

$$U_j \equiv -\sum_i f_i \, , \qquad \begin{cases} f_i = 1 & (r_{ij} \leq d) \\ f_i = 0 & (r_{ij} > d) \end{cases} \qquad (2)$$

where U_j is the artificial potential at surface point j, and U_j is defined as the negative value of the total number of grid points of material with distance $r \leq d$. We used this simple model for the surface potential calculations to focus on the shape of the mixture in discrete grid space. An equilibrium mixing state was simulated assuming that the applied WS components preferentially accumulate at grid points of lower potential. The shape of internally mixed particles under an arbitrary volume mixing ratio was determined based on iterative calculations of the surface potential and by adding WS elements. In the artificial potential calculations in Eq. (2), setting of the length d is important. We applied two steps for the potential calculations and adhesion of WS components for each iterative calculation.

$$d_1 = 3l \, , \qquad N_{\mathrm{add}} = 0.016 N_s$$
$$d_2 = Max(d_1, d_{cor}) \, , \quad N_{\mathrm{add}} = 0.004 N_s, \qquad (3)$$

where l is the grid length of the space, d_1 and d_2 are the lengths d for first and second steps, and N_{add} is the number of grid points for WS adhesion, which are chosen from the total surface points N_s (note that a surface point is defined as an empty grid and neighbor of an occupied grid). Small d_1 values resulted in a coated particle with a thin layer at a local scale. By contrast, WS components tended to accumulate in the same region on particles when a large d_1 was applied. <mark>We assumed the parameter d_1 to be the minimum scale to derive isotropic potential in the discrete Cartesian grid space and determined the value $d_1 = 3l$ from our results for shapes of coated particles in preliminary calculations.</mark> The second step in Eq. (3) is important, particularly when WS components cover the entire soot aggregate, and the value d_2 is determined to ensure that the overall shape of the mixed particle is spherical. The correction length d_{cor} is the minimum length at which the curvature of the sphere with a radius R can be discriminated from the calculated artificial potential in the grid field, and d_{cor} is estimated from the following relationships.

$$\frac{4}{3}\pi R^3 = N_V l^3 \, , \quad 4\pi R^2 \gamma = N_s l^3, \quad R \sin \theta = d_{cor} \, , \quad R \cos \theta = R - l \qquad (4)$$

$$d_{cor} = l \sqrt{\frac{6 N_V \gamma}{N_s l} - 1} \qquad (5)$$

where N_V is the total number of grid points occupied by the material, and γ is the effective skin depth ($\gamma = 1.51l$). Figure 3 presents a schematic diagram describing d_{cor} in a two-dimensional case.
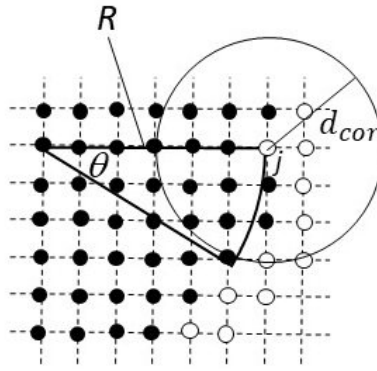
Figure 3. Schematic diagram of the distance d_{cor} based on the artificial potential calculation for a two-dimensional case. Open circles represent surface points for the potential field calculation, and solid circles indicate points occupied by material. To discriminate the curvature of the radius R from the calculated potential at surface point j, the length d in Eq. (2) should be larger than d_{cor}. A spherical mixed particle is automatically generated from the potential calculations and adding water-soluble material when the soot particle is completely encapsulated.

The artificial potential was calculated for each iterative step, and N_{add} of WS elements was added starting with the grid points of lowest potential. The internally mixed soot model (i.e., the particle shape modeled based on artificial surface tension, AST hereafter) was created for different values of the volume ratio $V_r = V_{ws}/V_{soot}$, where V_{ws} and V_{soot} are the volumes of the WS and soot materials, respectively. Figure 4 shows the results of several mixed soot models for $V_r \sim 0, 2, 5, 10, 20$. The total number of iterations was approximately 1000 (2000) to create $V_r \sim 10$ ($V_r \sim 20$) particles. For simplicity, we neglected the difference in materials (i.e., soot or WS) in the potential calculations of Eq. (2), which implicitly assumes that soot material is sufficiently hydrophilic, with high WS wettability. Although we made assumptions in the modeling of these particles, their shapes are similar to those observed by electron microscopy (Adachi et al., 2010; Fig. 5). The shape model of the particle was ultimately defined using a three-dimensional rendering technique.
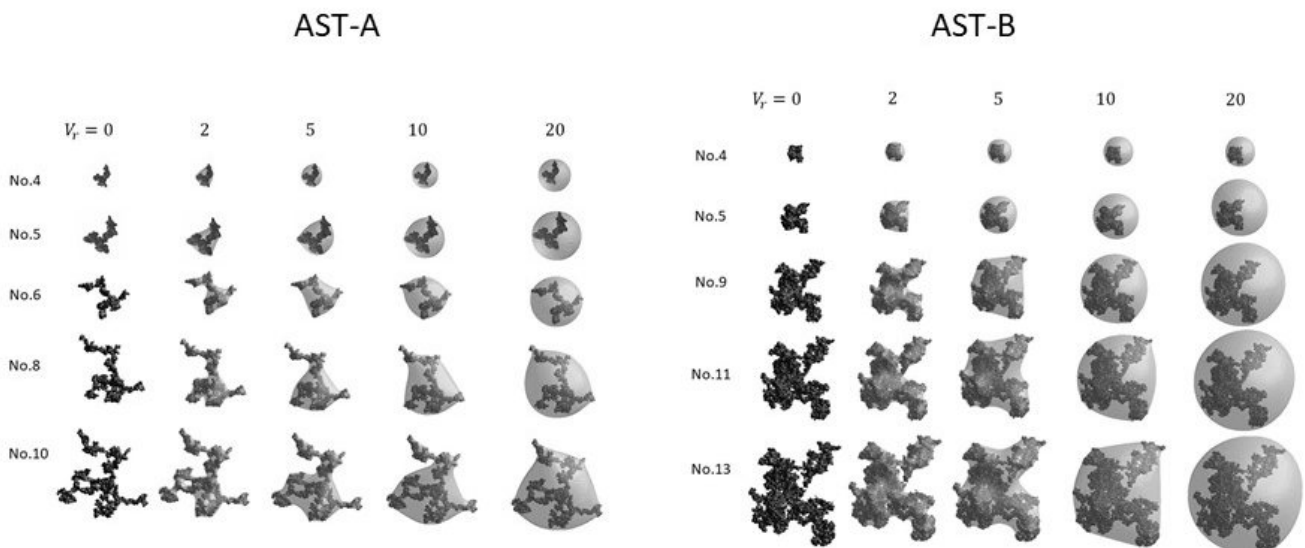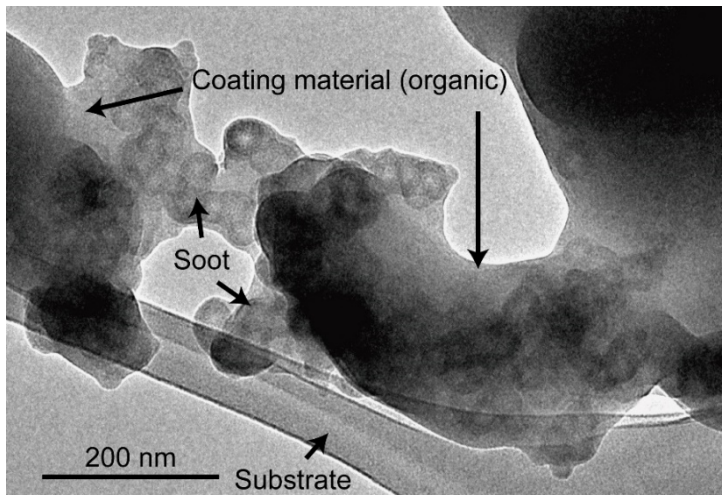

Figure 4. Mixed soot particle model developed using artificial surface tension (AST) for the attached water-soluble material. Several Type A (Type B) aggregates of different sizes were used on the left (right) side. The marching cubes method was applied for surface rendering.

5

Figure 5. An example transmission electron microscopy (TEM) image of an internally mixed soot particle. The sample was collected from biomass burned during the Biomass Burning Observation Project (BBOP)(Adachi et al., 2018). The soot particle has an aggregate structure of spherical monomers and is embedded within organic material. This particle looks similar to the AST-A particles (e.g., No. 6 particle with $V_r = 5$ in Figure 4).

3 Single-scattering properties

We calculated the light-scattering properties using the finite-difference time-domain (FDTD) method (Cole, 2005)(Taflove and Hagness, 2005) (Ishimoto et al., 2012a) and DDA [DDSCAT ver.7.3, http://www.ddscat.org/ (Draine and Flatau, 1994)]. Particles defined by discrete points as the input for the light-scattering calculations were reconstructed from the shape model described in Section 2, and the grid length was set within the range $2 \leq 2a/l \leq 10$ for correct reproduction of the defined aggregates within the numerical convergence criterion. Although soot particles are generally small aerosols, large computational resources for FDTD and DDA calculations are necessary to estimate the exact scattering properties of the mixed particles due to the fine structure of soot and additional volume contributed by WS material. Using the same discretized particle under an appropriate convergence condition, the scattering properties calculated by FDTD would have approximately the same accuracy as those derived from DDA (Yurkin et al., 2007). However, the numerical cost of the two methods differs depending on the particle shape and the refractive index of the particle material (Yurkin et al., 2007). The memory and CPU time of the DDA calculations mainly depend on the number of discretized points (i.e., dipoles) and depend on particle volume. Meanwhile, the numerical costs of the FDTD calculations are determined by the size of the discretized numerical field that encloses the particle. For fractal-shaped particles of relatively small fractal dimensions, DDA calculations are faster than FDTD ones because of the small relative volume with respect to size. By contrast, the numerical cost of DDA calculations drastically increases as the volume of attached WS elements increases, whereas the FDTD method can output results within similar CPU times given similar total sizes. Therefore, we used both numerical methods for the light-scattering calculations in accordance with the size and shape of the particles. In the numerical environment of our non-parallel computation, light scattering calculations performed using FDTD were faster than those using DDA for AST-B particles (Nos.10–13).

As indicated in Section 2 and shown in Figures 1 and 2, 10 sizes of bare soot aggregates with a volume-equivalent sphere radius $r_{eq} = 0.02 - 0.20$ μm for Type-A and 13 sizes with $r_{eq} = 0.02 - 0.42$ μm for Type-B were prepared, and internally mixed particles of $V_r \sim 0, 2, 5, 10, 20$ were numerically created for each soot particle. The corresponding size ranges of the mixed soot particles were $r_{eq} = 0.02 - 0.55$ μm for Type-A (AST-A) and $r_{eq} = 0.02 - 1.15$ μm for Type-B (AST-B). Assuming a synthetic analysis using satellite-/ground-based multi-channel radiometer and lidar measurements, 10 wavelengths

from near-ultraviolet to near-infrared (340, 355, 380, 400, 500, 532, 675, 870, 1020, 1064 nm) were selected. We used a spectral refractive index dataset by (Chang and Charalampopoulos, 1990) for the bare soot material. For the WS components, the dependence of the refractive index on relative humidity was considered, and relative humidity values of 0%, 50%, 90%, and 98% in the software package Optical Properties of Aerosols and Clouds (OPAC) were applied (Hess et al., 1998). The outputs included the results of the light-scattering properties with those averaged over 88 orientations for the FDTD method and 100 orientations for the DDA method.

As examples of the numerical results, Figures 6 and 7 present the size (r_{eq}) dependence of single-scattering albedo (ω) and the asymmetry factor (g) at wavelength of $\lambda = 532$ nm for AST-A. The complex refractive indices for soot and WS are listed in Table 1, where the refractive index at a relative humidity of 50% were applied for WS. For comparison, the results of ω and g with the same V_r but derived via Mie calculations for spheres of the effective refractive index calculated using the Maxwell–Garnett mixing rule (MG) (Bohren and Huffman, 1983) and for spheres with a soot-core/WS-shell structure (CS) were also plotted.

For ω and g at $\lambda = 532$ nm, the results of the AST model were approximately consistent with previous modeled results (Dong et al., 2015)(Liu et al., 2016). The results of ω for AST-A at $V_r = 0$ markedly differed from those of MG/CS due to the volume-equivalent sphere approximation adopted in the MG/CS treatments. The results of ω for AST-A with $V_r \geq 2$ showed a similar trend to the MG/CS results such that the MG results were closer to AST-A than was CS. Regarding the asymmetry factor, g depends mainly on the particle size r_{eq} and is less sensitive to the mixing ratio V_r. The derived g for AST-A fell between the results of MG and of CS, with the MG results closer to those of AST-A. Because the primary particle of the assumed soot ($a = 0.02$ μm) was smaller than the wavelength and the Type A aggregates were fractal shapes with relatively small D_f (Figs. 1 and 2), the effective medium theory based on the MG mixing rule offered a better approximation than did the CS approximation for the AST-A model.

Table 1. Complex refractive index ($n + i\,k$) of soot and water-soluble components (WS) used for light scattering calculations (Figs. 6–10). A relative humidity of 50% was assumed for the WS component.

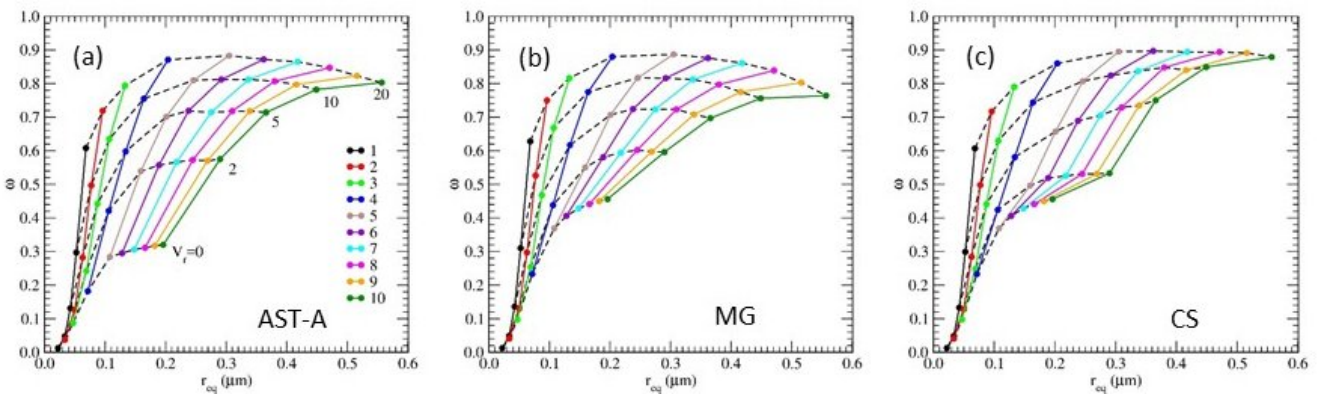| wavelength (nm)	soot		water soluble	
	n	k	n	k
355	1.392	0.6985	1.441	2.469×10^{-3}
532	1.723	0.5837	1.437	2.982×10^{-3}
1064	1.830	0.5573	1.427	8.691×10^{-3}

Figure 6. Single-scattering albedo ω versus particle size (volume-equivalent sphere radius: r_{eq}) at a wavelength of $\lambda = 532$ nm for the (a) AST model of Type A aggregates (AST-A), (b) Maxwell–Garnett approximation (MG), and (c) core-shell approximation (CS). Results for the same bare soot aggregate at different volume ratios of $V_r \sim 0, 2, 5, 10, 20$ are plotted in the same color. Aggregate numbers are the same as those in Figure 1.
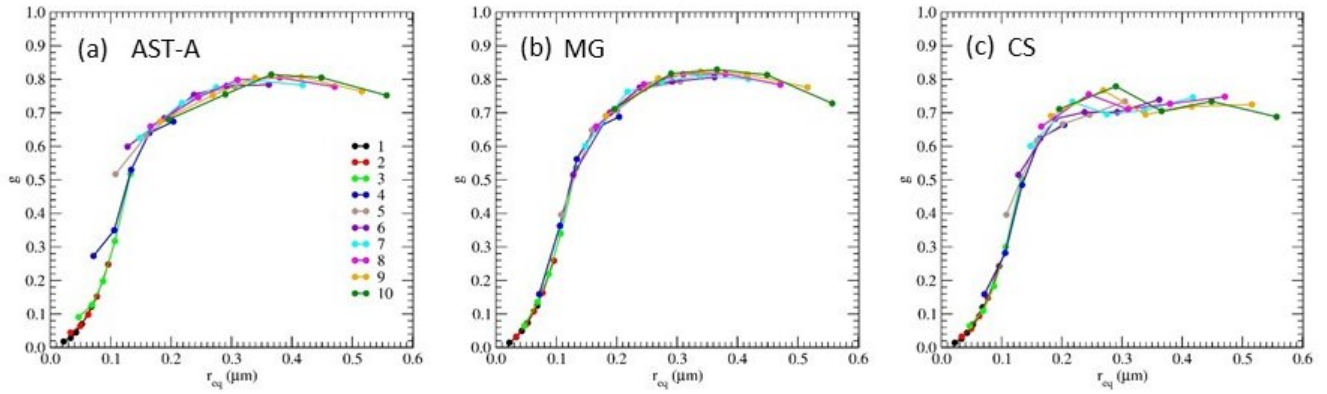

Figure 7. As Fig. 6, but for the results of the asymmetry factor g.

Compared to ω and g, the backscattering properties of particles are sensitive to particle shape and mixing state. Therefore, lidar measurements could potentially offer information on the validity of the particle model. The calculated lidar ratio L and linear depolarization ratio δ_L for the AST-A and AST-B particles at wavelengths of 355, 532, and 1064 nm are plotted in Figures 8–10. For a single particle, L is calculated from ω and the normalized phase function P_{11} in the backscattering direction, and δ_L is derived from the P_{11} and P_{22} components of the scattering matrix. Here, we omitted the backscattering of P_{12} for δ_L due to the assumption of random particle orientation.

$$L = \frac{4\pi}{\omega P_{11}}, \, \delta_L = \frac{P_{11} - P_{22}}{P_{11} + P_{22}}. \qquad (6)$$

For lidar ratios, the MG and CS sphere results for the same volume of bare soot aggregates and the same r_{eq} range of $V_r \le 20$ as that for AST-A and AST-B are also plotted in Figures 8 and 9. Because backscattering P_{11} is sensitive to the size for spherical particles, calculations were performed at a step size of 0.01 μm. The lidar ratios of CS particles tended to be smaller than those of MG particles, and the difference between MG and CS was significant at wavelengths of 355 nm and 532 nm. Furthermore, the lidar ratios of AST-A and AST-B particles were approximately between the MG and CS results for particles of the same r_{eq} and mixing ratios, particularly for entirely encapsulated $V_r \ge 10$ particles. As denoted in the asymmetry factor results, MG and CS corresponded to two extreme cases of mixture soot materials within the WS shell; our lidar ratio results for fractal-like soot shapes among AST-A and AST-B are reasonable.

Due to strong absorption properties, bare soot particles showed small depolarization ratios δ_L (Fig. 10). As the value V_r increased, δ_L of the AST particles increased through the mixing of weak absorbing material (i.e., WS), and δ_L began to decrease for larger values of V_r due to their spherical shape. This indicates that the smooth surface created by a thin WS coating was rather ineffective for reducing δ_L when the overall shape was highly non-spherical. As a result, AST particles of the same bare soot size as those shown in Figure 10 (data of same color) had a peak depolarization ratio. To some extent, peak values of δ_L were larger for larger bare soot particles at shorter wavelengths. This implies that the particle size parameter x_{eq} (= $2\pi r_{eq}/\lambda$) is an important factor for the evaluation of δ_L as well as shape non-sphericity.

According to the biomass smoke measurement results, the size of dry particles was 0.10–0.16 μm at count median diameter (0.25–0.30 μm at volume median diameter) (Reid et al., 2005a). Laboratory and *in situ* measurements for aged biomass smoke

yielded estimates of $\omega \geq 0.75$ and $g \sim 0.6$ at $\lambda = 532$ nm (Reid et al., 2005b)(Pokhrel et al., 2016). For lidar measurements, typical values of $L \sim 70$ sr and $\delta_L \sim 7$ % at $\lambda = 532$ nm have been reported (Groß et al., 2015a)(Groß et al., 2015b). Among our optical property results for AST-A, particle No. 4 ($V_r = 20$) had values of $(\omega, g, L, \delta_L) = (0.87, 0.67, 69 \text{ sr}, 0 \text{ %})$, and particle No.5 ($V_r = 2$) had values of $(\omega, g, L, \delta_L) = (0.54, 0.63, 188 \text{ sr}, 6 \text{ %})$. Using the refractive index of a typical soot

5 particle, relatively high values of V_r would be necessary to simulate $\omega \geq 0.75$. In the AST model, the soot aggregate was entirely encapsulated by WS components, and the overall shape became spherical under large V_r values. Although such spherical particles have consistent lidar ratios of $L \sim 70$ sr, the depolarization ratio becomes $\delta_L \sim 0$ for spherical shapes. By contrast, large depolarization ratios can occur if internally mixed particles are highly non-spherical. Moreover, the reported spectral dependence of depolarization ratios $(\delta_{L,355nm} \sim 20 \text{ %}, \; \delta_{L,532nm} \sim 9 \text{ %}, \delta_{L,1064nm} \sim 2 \text{ %})$ from airborne measurements

10 for smoke plumes (Burton et al., 2015) (Mishchenko et al., 2016) can be explained, for example, by the AST-A particle No. 6 ($V_r = 5 - 10$; Fig. 10a–c). However, such non-spherical mixed particles tended to have relatively large lidar ratios of $L \geq 100$ sr at $\lambda = 355, 532$ nm in the AST-A model. In the comparison between AST-A and AST-B particles, variation in L and δ_L for AST-B were greater than those for AST-A. At $\lambda = 355$ nm, the measurement-derived lidar ratio was $L_{355nm} = 76 \pm 12$ sr (Groß et al., 2015b). The value was difficult to explain for MG particles, but was relatively consistent with the large V_r

15 observed for AST-A/-B particles and some CS particles. By contrast, the calculated depolarization ratios of AST-A and AST-B particles at both $\lambda = 355$ nm and 532 nm exceeded 30% for larger aggregates with a high amount of coating. These ratios were higher than those measured for biomass burning [7~16% (Groß et al., 2015b)], suggesting that the depolarization ratios of non-spherical soot particles were easily enhanced when coated with weakly absorbing WS material. A similar effect was previously reported (Kahnert, 2017). According to (Kanngießer and Kahnert, 2018), the speed of transition from film coating

20 to spherical growth (Pei et al., 2018) is a morphological parameter that strongly affects the depolarization ratio. A rapid transition to spherical growth may cause a smaller depolarization ratio of internally mixed soot particles.

Overall, the results shown in Figures 8–10 suggest that the effects of internal mixing on lidar backscattering are strongly related to changes in absorption/shape properties due to mixing and bare soot particle size. However, it was difficult to simulate average smoke optical properties (ω, g, L, δ_L) and their spectral dependence solely using AST-A or AST-B particles.

25 Among the field measurements, the observed optical properties were the average of the particle size distribution. Our results indicate that the presence of large mixed soot particles may enhance the bulk δ_L of smoke.

Typical values of V_r for mixed biomass smoke particles likely depend on the relative humidity, concentrations of WS components, and size/shape of soot aggregates. The mixing of different aerosol types, such as dust in biomass burning (Groß et al., 2011)(Groß et al., 2013), may be important for the interpretation of measured optical properties. Improved retrieval

30 calculations based on realistic aerosol simulations that consider particle size/shape distribution and other types of aerosol contamination are expected using our AST model for internally mixed soot particles.
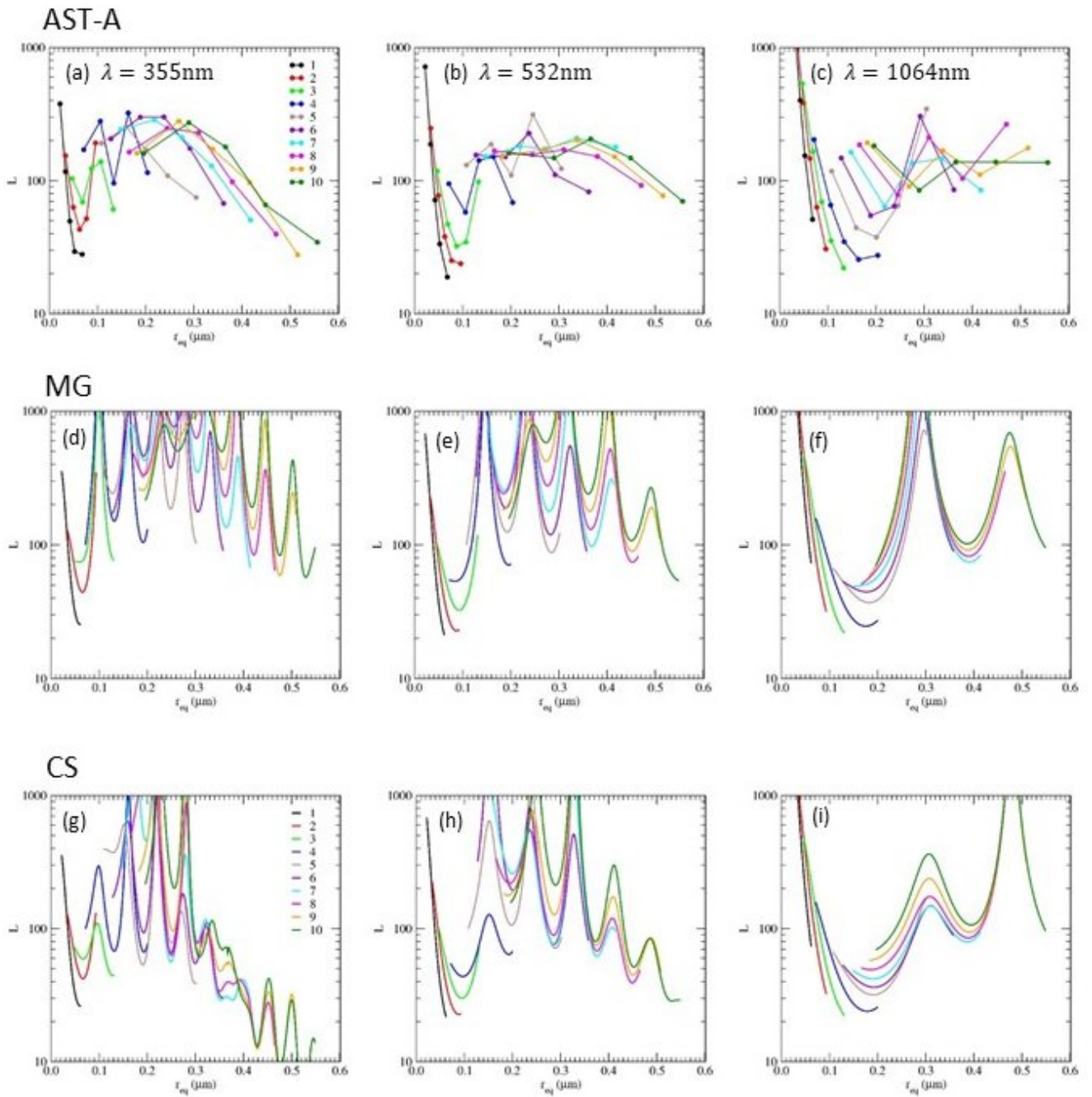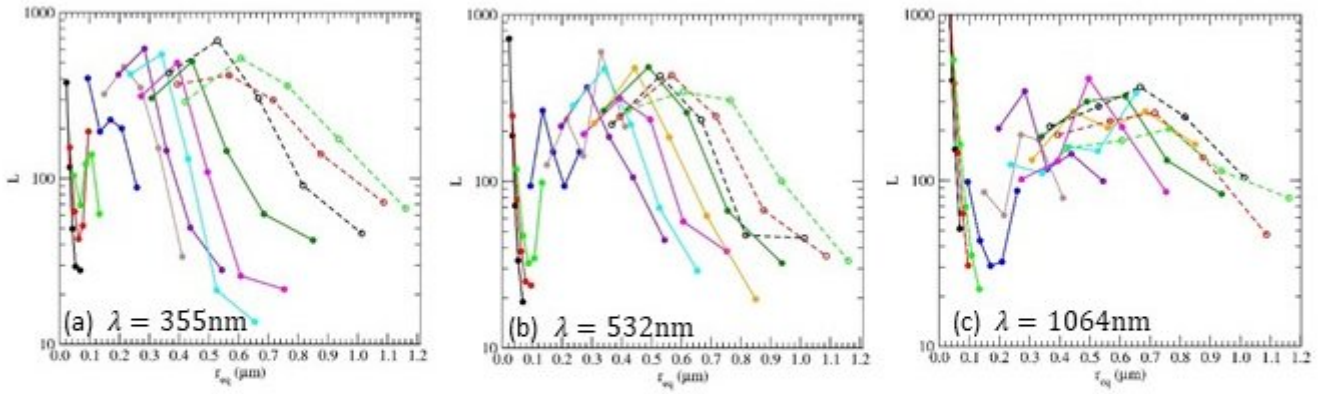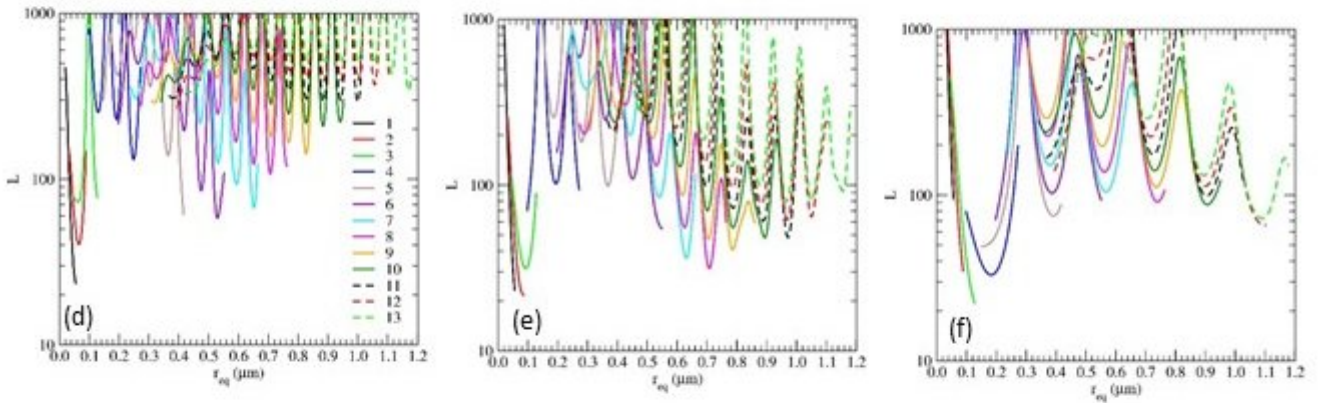
Figure 8. Results of the lidar ratio L for particles derived from the AST-A model at wavelengths of (a) 355, (b) 532, and (c) 1064 nm. (d–f) As a–c, but for spheres with an average refractive index calculated using the Maxwell–Garnett mixing rule (MG). (g–i) As a–c but for core-shell spheres (CS). Colors and volume ratios V_r for each point are the same as those in Figure 6a for the AST-A model ($V_r \sim 0, 2, 5, 10, 20$ from left to right for circles of the same color). For (d–i), calculations were performed for $V_r \leq 20$ with a step size of 0.01 μm.
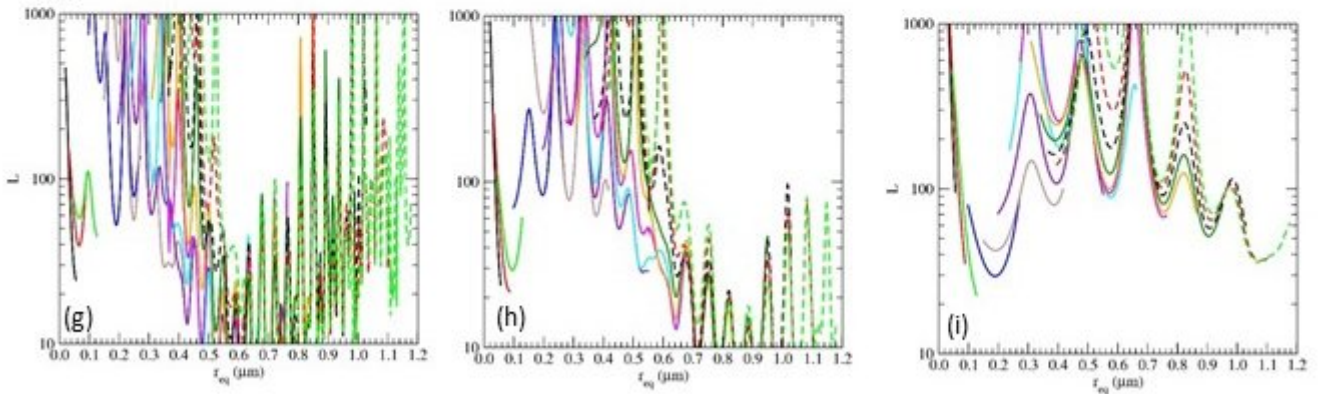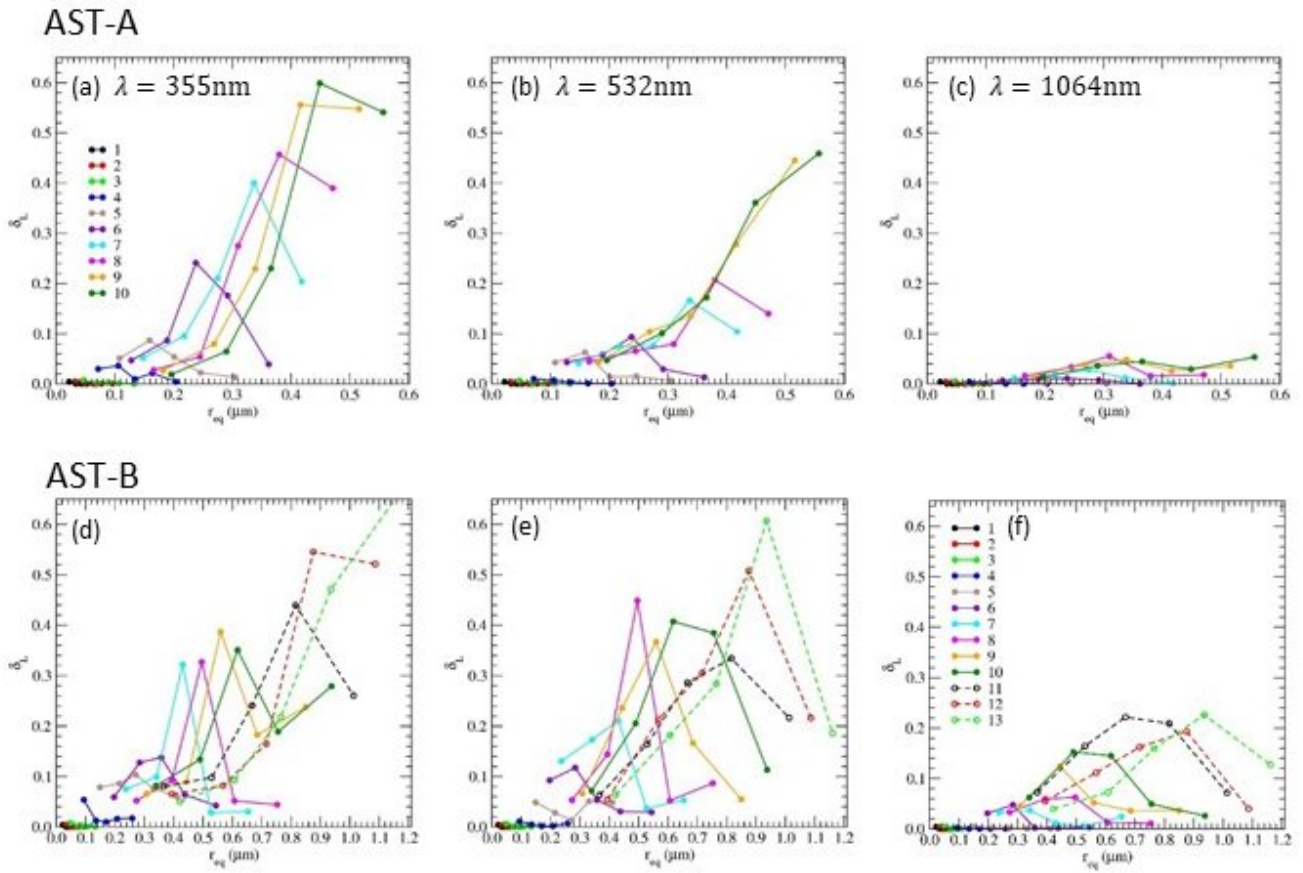
5

Figure 9. As Fig. 8, but for internally mixed Type B particles (AST-B) (a–c), MG (d–f), and CS (g–i). The horizontal scale differs from that shown in Figure 8.

5

10

11

Figure 10. Results of the linear depolarization ratio δ_L for particles derived from the AST-A model at wavelengths of (a) 355, (b) 532, and (c) 1064 nm. (d–f) As (a–c), but for AST-B particle results.

5 Summary

For satellite-/ground-based remote-sensing analysis applications, we developed a shape model of internally mixed soot particles and calculated the optical properties of particles at visible and near-infrared wavelengths. Fractal-like structures extracted using spatial Voronoi tessellation were considered to mimic necking and overlapping between neighboring primary particles. We created two types of polyhedral aggregates with different particle shape–size dependences (Type-A and Type-B) to account for the effects of compaction on soot aggregate shape during the atmospheric aging process. Then the artificial surface potential for the particle in a Cartesian grid space was defined, and the surface tension of the WS components on the soot aggregate was simulated, assuming that the soot was hydrophilic with high wettability. Based on a simple assumption of the behavior of WS elements, the shapes of internally mixed soot particles dependent on the amount of attached dissolved material were determined from iterative calculations. Overall, an aggregate coated with a thin film was simulated given a relatively small volume of added WS components, whereas the soot aggregate was covered with a spherical shell given a large amount of WS components. The optical properties of the developed internally mixed particles were calculated using the FDTD and DDA methods while considering the spectral dependence on the refractive indices.

For single-scattering albedo and asymmetry, AST model results were similar to those for MG and CS, except when the WS ratio was low ($V_r \sim 0$). Due to shape irregularities, the lidar ratios of AST particles in random orientation were less sensitive to particle size than those of MS and CS particles. The L values of AST particles were approximately between those of MG and CS particles. For AST particles, δ_L increased as the amount of weakly absorbing material (i.e., WS) increased, and δ_L decreased as particle shape became spherical. As a result, irregularly shaped soot particles had peak depolarization ratios during the internal mixing process. Maximum δ_L values tended to be larger when the size parameters of non-spherical mixed particles were large. Following comparisons with reported optical features, we determined that average optical properties (ω, g, L, δ_L) and their spectral dependences for measured biomass burning aerosols cannot be simulated by a single particle in our internally mixed soot model. In particular, AST particles tended to have larger lidar ratios and depolarization ratios than those obtained by field measurements. The inconsistencies in lidar backscattering properties between the model results and measurements may remain unresolved even after size-averaging the optical properties. One possible explanation for this phenomenon is that soot aggregates change their shapes to become more compact (i.e., become spherical) during the WS adhesion process in the atmosphere. The contribution of the core shell type of internally mixed soot particles and the use of the non-spherical model may be necessary to simulate observed results for burned biomass aerosols.

In addition to its use in direct analyses for the field measurement results, the dataset of the AST particle optical properties can be used for the parameterization of conventional spherical particle models, such as the MG model, CS model, and their combined model. Furthermore, the dataset will be useful for determining the shape property conditions of smoke particles observed from multi-sensor measurements, including lidar backscattering.

References

Adachi, K. and Buseck, P. R.: Internally mixed soot, sulfates, and organic matter in aerosol particles from Mexico City, Atmos. Chem. Phys., 8(21), 6469–6481, doi:10.5194/acp-8-6469-2008, 2008.

Adachi, K., Chung, S. H., Friedrich, H. and Buseck, P. R.: Fractal parameters of individual soot particles determined using electron tomography: Implications for optical properties, J. Geophys. Res. Atmos., 112(14), 1–10, doi:10.1029/2006JD008296, 2007.

Adachi, K., Chung, S. H. and Buseck, P. R.: Shapes of soot aerosol particles and implications for their effects on climate, J. Geophys. Res. Atmos., 115(15), 1–9, doi:10.1029/2009JD012868, 2010.

Adachi, K., Sedlacek, A. J., Kleinman, L., Chand, D., Hubbe, J. M. and Buseck, P. R.: Volume changes upon heating of aerosol particles from biomass burning using transmission electron microscopy, Aerosol Sci. Technol., 52(1), 46–56, doi:10.1080/02786826.2017.1373181, 2018.

Akinci, N., Akinci, G. and Teschner, M.: Versatile surface tension and adhesion for SPH fluids, ACM Trans. Graph., doi:10.1145/2508363.2508395, 2013.

Baran, A. J., Ishimoto, H., Sourdeval, O., Hesse, E. and Harlow, C.: The applicability of physical optics in the millimetre and sub-millimetre spectral region. Part II: Application to a three-component model of ice cloud and its evaluation against the

bulk single-scattering properties of various other aggregate models, J. Quant. Spectrosc. Radiat. Transf., 206, 83–100, doi:10.1016/j.jqsrt.2017.10.027, 2018.

Becker, S., Urbassek, H. M., Horsch, M. and Hasse, H.: Contact Angle of Sessile Drops in Lennard-Jones Systems, , doi:10.1021/la503974z, 2014.

5 Bohren, C. F. and Huffman, D. R.: Absorption and scattering of light by small particles, John Wiley & Sons., 1983.

Bond, T. C. and Bergstrom, R. W.: Light absorption by carbonaceous particles: An investigative review, Aerosol Sci. Technol., 40(1), 27–67, doi:10.1080/02786820500421521, 2006.

Burton, S. P., Hair, J. W., Kahnert, M., Ferrare, R. A., Hostetler, C. A., Cook, A. L., Harper, D. B., Berkoff, T. A., Seaman, S. T., Collins, J. E., Fenn, M. A. and Rogers, R. R.: Observations of the spectral dependence of linear particle depolarization

10 ratio of aerosols using NASA Langley airborne High Spectral Resolution Lidar, Atmos. Chem. Phys., 15(23), 13453–13473, doi:10.5194/acp-15-13453-2015, 2015.

Chang, H. and Charalampopoulos, T. T.: Determination of the Wavelength Dependence of Refractive Indices of Flame Soot, Proc. R. Soc. A Math. Phys. Eng. Sci., 430(1880), 577–591, doi:10.1098/rspa.1990.0107, 1990.

Cheng, T., Gu, X., Wu, Y. and Chen, H.: Effects of atmospheric water on the optical properties of soot aerosols with

15 different mixing states, J. Quant. Spectrosc. Radiat. Transf., 147, 196–206, doi:10.1016/j.jqsrt.2014.06.002, 2014.

Cole, J. B.: High accuracy nonstandard finite-difference time-domain algorithms for computational electromagnetics: Applications to optics and photonics, in Advances in the Applications of Nonstandard Finite Difference Schemes, edited by R. E. Mickens, pp. 89–189, World Scientific., 2005.

Dong, J., Zhao, J. M. and Liu, L. H.: Morphological effects on the radiative properties of soot aerosols in different internally

20 mixing states with sulfate, J. Quant. Spectrosc. Radiat. Transf., 165, 43–55, doi:10.1016/j.jqsrt.2015.06.025, 2015.

Draine, B. T. and Flatau, P. J.: Discrete-Dipole Approximation For Scattering Calculations, J. Opt. Soc. Am. A, 11(4), 1491, doi:10.1364/JOSAA.11.001491, 1994.

Groß, S., Tesche, M., Freudenthaler, V., Toledano, C., Wiegner, M., Ansmann, A., Althausen, D. and Seefeldner, M.: Characterization of Saharan dust, marine aerosols and mixtures of biomass-burning aerosols and dust by means of multi-

25 wavelength depolarization and Raman lidar measurements during SAMUM 2, Tellus, Ser. B Chem. Phys. Meteorol., 63(4), 706–724, doi:10.1111/j.1600-0889.2011.00556.x, 2011.

Groß, S., Esselborn, M., Weinzierl, B., Wirth, M., Fix, A. and Petzold, A.: Aerosol classification by airborne high spectral resolution lidar observations, Atmos. Chem. Phys., 13(5), 2487–2505, doi:10.5194/acp-13-2487-2013, 2013.

Groß, S., Freudenthaler, V., Schepanski, K., Toledano, C., Schäfler, A., Ansmann, A. and Weinzierl, B.: Optical properties

30 of long-range transported Saharan dust over Barbados as measured by dual-wavelength depolarization Raman lidar measurements, Atmos. Chem. Phys., 15(19), 11067–11080, doi:10.5194/acp-15-11067-2015, 2015a.

Groß, S., Freudenthaler, V., Wirth, M. and Weinzierl, B.: Towards an aerosol classification scheme for future EarthCARE lidar observations and implications for research needs, Atmos. Sci. Lett., 16(1), 77–82, doi:10.1002/asl2.524, 2015b.

Hara, Y., Nishizawa, T., Sugimoto, N., Osada, K., Yumimoto, K., Uno, I., Kudo, R. and Ishimoto, H.: Retrieval of Aerosol

35 Components Using Multi-Wavelength Mie-Raman Lidar and Comparison with Ground Aerosol Sampling, Remote Sens., 10(6), 937, doi:10.3390/rs10060937, 2018.

He, C., Liou, K. N., Takano, Y., Zhang, R., Levy Zamora, M., Yang, P., Li, Q. and Leung, L. R.: Variation of the radiative properties during black carbon aging: Theoretical and experimental intercomparison, Atmos. Chem. Phys., 15(20), 11967–11980, doi:10.5194/acp-15-11967-2015, 2015.

40 Hess, M., Koepke, P. and Schult, I.: Optical Properties of Aerosols and Clouds: The Software Package OPAC, Bull. Am. Meteorol. Soc., 79(5), 831–844, doi:10.1175/1520-0477(1998)079<0831:OPOAAC>2.0.CO;2, 1998.

Ishimoto, H., Zaizen, Y., Uchiyama, A., Masuda, K. and Mano, Y.: Shape modeling of mineral dust particles for light-scattering calculations using the spatial Poisson-Voronoi tessellation, J. Quant. Spectrosc. Radiat. Transf., 111(16), 2434–2443, doi:10.1016/j.jqsrt.2010.06.018, 2010.

Ishimoto, H., Masuda, K., Mano, Y., Orikasa, N. and Uchiyama, A.: Irregularly shaped ice aggregates in optical modeling of convectively generated ice clouds, J. Quant. Spectrosc. Radiat. Transf., 113(8), 632–643, doi:10.1016/j.jqsrt.2012.01.017, 2012a.

Ishimoto, H., Zaizen, Y., Masuda, K., Mano, Y. and Uchiyama, A.: Shape modeling of dust and soot particles for remote sensing applications considering the geometrical features of sampled aerosols, in Technical Reports of the Meteorological Research Institute, pp. 40–43. [online] Available from: http://www.mri-jma.go.jp/Publish/Technical/index_en.html, 2012b.

Jacobson, M. Z.: Strong radiative heating due to the mixing state of black carbon in atmospheric aerosols, Nature, 409(6821), 695–697, doi:10.1038/35055518, 2001.

Kahnert, M.: Optical properties of black carbon aerosols encapsulated in a shell of sulfate: comparison of the closed cell model with a coated aggregate model, Opt. Express, 25(20), 24579, doi:10.1364/OE.25.024579, 2017.

Kahnert, M., Nousiainen, T. and Lindqvist, H.: Models for integrated and differential scattering optical properties of encapsulated light absorbing carbon aggregates, Opt. Express, 21(7), 7974–7993, 2013.

Kanngießer, F. and Kahnert, M.: Journal of Quantitative Spectroscopy & Radiative Transfer Calculation of optical properties of light-absorbing carbon with weakly absorbing coating : A model with tunable transition from film-coating to spherical-shell coating, , 216, 17–36, doi:10.1016/j.jqsrt.2018.05.014, 2018.

Leinonen, J. and von Lerber, A.: Snowflake Melting Simulation Using Smoothed Particle Hydrodynamics, J. Geophys. Res. Atmos., 123(3), 1811–1825, doi:10.1002/2017JD027909, 2018.

Liu, F., Yon, J. and Bescond, A.: On the radiative properties of soot aggregates - Part 2: Effects of coating, J. Quant. Spectrosc. Radiat. Transf., 172, 134–145, doi:10.1016/j.jqsrt.2015.08.005, 2016.

Luo, J., Zhang, Y. and Zhang, Q.: A model study of aggregates composed of spherical soot monomers with an acentric carbon shell, J. Quant. Spectrosc. Radiat. Transf., 205, 184–195, doi:10.1016/j.jqsrt.2017.10.024, 2018.

Mikhailov, E. F., Vlasenko, S. S., Krämer, L. and Niessner, R.: Interaction of soot aerosol particles with water droplets: Influence of surface hydrophilicity, J. Aerosol Sci., 32(6), 697–711, doi:10.1016/S0021-8502(00)00101-4, 2001.

Mikhailov, E. F., Vlasenko, S. S., Podgorny, I. A., Ramanathan, V. and Corrigan, C. E.: Optical properties of soot-water drop agglomerates: An experimental study, J. Geophys. Res. Atmos., 111(7), doi:10.1029/2005JD006389, 2006.

Mishchenko, M. I., Dlugach, J. M. and Liu, L.: Linear depolarization of lidar returns by aged smoke particles, Appl. Opt., 55(35), 9968–9973, doi:10.1364/AO.55.009968, 2016.

Moteki, N.: Discrete dipole approximation for black carbon-containing aerosols in arbitrary mixing state: A hybrid discretization scheme, J. Quant. Spectrosc. Radiat. Transf., 178, 306–314, doi:10.1016/j.jqsrt.2016.01.025, 2016.

Nyeki, S. and Colbeck, I.: Fractal Dimension Analysis of Single, In-Situ, Restructured Carbonaceous Aggregates, Aerosol Sci. Technol., 23(2), 109–120, doi:10.1080/02786829508965298, 1995.

Ohser, J. and Mücklich, F.: Statistical Analysis of Microstructures in Materials Science, John Wiley & Sons., 2000.

Okyay, G., Héripré, E., Reiss, T., Haghi-Ashtiani, P., Auger, T. and Enguehard, F.: Soot aggregate complex morphology: 3D geometry reconstruction by SEM tomography applied on soot issued from propane combustion, J. Aerosol Sci., 93, 63–79, doi:10.1016/j.jaerosci.2015.11.009, 2016.

Pei, X., Hallquist, M., Eriksson, A. C., Pagels, J., Donahue, N. M., Mentel, T., Svenningsson, B., Brune, W. and Pathak, R. K.: Morphological transformation of soot: Investigation of microphysical processes during the condensation of sulfuric acid and limonene ozonolysis product vapors, Atmos. Chem. Phys., 18(13), 9845–9860, doi:10.5194/acp-18-9845-2018, 2018.

Pokhrel, R. P., Wagner, N. L., Langridge, J. M., Lack, D. A., Jayarathne, T., Stone, E. A., Stockwell, C. E., Yokelson, R. J. and Murphy, S. M.: Parameterization of single-scattering albedo (SSA) and absorption Ångström exponent (AAE) with

EC/OC for aerosol emissions from biomass burning, Atmos. Chem. Phys., 16(15), 9549–9561, doi:10.5194/acp-16-9549-2016, 2016.

Ramanathan, V., Carmichael, G., V. Ramanathan and G. Carmichael, Ramanathan, V. and Carmichael, G.: Global and regional climate changes due to black carbon, Nat. Geosci., 1(4), 221–227, doi:10.1038/ngeo156, 2008.

5   Reid, J. S., Koppmann, R., Eck, T. F. and Eleuterio, D. P.: A review of biomass burning emissions, part II: Intensive physical properties of biomass burning particles, Atmos. Chem. Phys., 5, 799–825, doi:10.5194/acpd-4-5135-2004, 2005a.

Reid, J. S., Eck, T. F., Christopher, S. A., Koppmann, R., Dubovik, O., Eleuterio, D. P., Holben, B. N., Reid, E. A. and Zhang, J.: A review of biomass burning emissions part III: intensive optical properties of biomass burning particles, Atmos. Chem. Phys., 5, 827–849, doi:10.5194/acpd-4-5201-2004, 2005b.

10   Reid, S. and Hobbs, P. V: Physical and optical properties of young smoke from individual biomass fires in Brazil, J. Geophys. Res., 103(D24), 32013–32030, 1998.

Scarnato, B., Vahidinia, S., Richard, D. T. and Kirchstetter, T. W.: Effects of internal mixing and aggregate morphology on optical properties of black carbon using a discrete dipole approximation model, Atmos. Chem. Phys. Discuss., 12(10), 26401–26434, doi:10.5194/acpd-12-26401-2012, 2012.

15   Shiraiwa, M., Kondo, Y., Moteki, N., Takegawa, N., Miyazaki, Y. and Blake, D. R.: Evolution of mixing state of black carbon in polluted air from Tokyo, Geophys. Res. Lett., 34(16), 2–6, doi:10.1029/2007GL029819, 2007.

Shiraiwa, M., Kondo, Y., Iwamoto, T. and Kita, K.: Amplification of light absorption of black carbon by organic coating, Aerosol Sci. Technol., 44(1), 46–54, doi:10.1080/02786820903357686, 2010.

Taflove, A. and Hagness, S. C.: Computational electrodynamics The finite-difference time-domain method, 3rd ed., Artech
20   House., 2005.

Tartakovsky, A. and Meakin, P.: Modeling of surface tension and contact angles with smoothed particle hydrodynamics, Phys. Rev. E, 72(2), 026301, doi:10.1103/PhysRevE.72.026301, 2005.

Wu, Y., Cheng, T., Zheng, L., Chen, H. and Xu, H.: Single scattering properties of semi-embedded soot morphologies with intersecting and non-intersecting surfaces of absorbing spheres and non-absorbing host, J. Quant. Spectrosc. Radiat. Transf.,
25   157, 1–13, doi:10.1016/j.jqsrt.2015.02.006, 2015.

Wu, Y., Cheng, T., Zheng, L. and Chen, H.: Optical properties of the semi-external mixture composed of sulfate particle and different quantities of soot aggregates, J. Quant. Spectrosc. Radiat. Transf., 179, 139–148, doi:10.1016/j.jqsrt.2016.03.012, 2016.

Wu, Y., Cheng, T., Zheng, L. and Chen, H.: Sensitivity of mixing states on optical properties of fresh secondary organic
30   carbon aerosols, J. Quant. Spectrosc. Radiat. Transf., 195, 147–155, doi:10.1016/j.jqsrt.2017.01.013, 2017.

Yon, J., Bescond, A. and Liu, F.: On the radiative properties of soot aggregates part 1: Necking and overlapping, J. Quant. Spectrosc. Radiat. Transf., 162, 197–206, doi:10.1016/j.jqsrt.2015.03.027, 2015.

Yurkin, M. A., Hoekstra, A. G., Brock, R. S. and Lu, J. Q.: Systematic comparison of the discrete dipole approximation and the finite difference time domain method for large dielectric scatterers, Opt. Express, 15(26), 17902–17911, 2007.

35   Zhang, X., Mao, M., Yin, Y. and Wang, B.: Absorption enhancement of aged black carbon aerosols affected by their microphysics: A numerical investigation, J. Quant. Spectrosc. Radiat. Transf., 202, 90–97, doi:10.1016/j.jqsrt.2017.07.025, 2017.

Zhang, Y., Zhang, Q., Cheng, Y., Su, H., Kecorius, S., Wang, Z., Wu, Z., Hu, M., Zhu, T., Wiedensohler, A. and He, K.: Measuring the morphology and density of internally mixed black carbon with SP2 and VTDMA: New insight into the
40   absorption enhancement of black carbon in the atmosphere, Atmos. Meas. Tech., 9(4), 1833–1843, doi:10.5194/amt-9-1833-2016, 2016.